LETTER

doi:10.1038/nature22060

Discovery of intrinsic ferromagnetism in two-dimensional van der Waals crystals

Cheng Gong[1]*, Lin Li[2]*, Zhenglu Li[3,4]*, Huiwen Ji[5], Alex Stern[2], Yang Xia[1], Ting Cao[3,4], Wei Bao[1], Chenzhe Wang[1], Yuan Wang[1,4], Z. Q. Qiu[3], R. J. Cava[5], Steven G. Louie[3,4], Jing Xia[2] & Xiang Zhang[1,4]

The realization of long-range ferromagnetic order in two-dimensional van der Waals crystals, combined with their rich electronic and optical properties, could lead to new magnetic, magnetoelectric and magneto-optic applications[1–4]. In two-dimensional systems, the long-range magnetic order is strongly suppressed by thermal fluctuations, according to the Mermin–Wagner theorem[5]; however, these thermal fluctuations can be counteracted by magnetic anisotropy. Previous efforts, based on defect and composition engineering[6–10], or the proximity effect, introduced magnetic responses only locally or extrinsically. Here we report intrinsic long-range ferromagnetic order in pristine $Cr_2Ge_2Te_6$ atomic layers, as revealed by scanning magneto-optic Kerr microscopy. In this magnetically soft, two-dimensional van der Waals ferromagnet, we achieve unprecedented control of the transition temperature (between ferromagnetic and paramagnetic states) using very small fields (smaller than 0.3 tesla). This result is in contrast to the insensitivity of the transition temperature to magnetic fields in the three-dimensional regime. We found that the small applied field leads to an effective anisotropy that is much greater than the near-zero magnetocrystalline anisotropy, opening up a large spin-wave excitation gap. We explain the observed phenomenon using renormalized spin-wave theory and conclude that the unusual field dependence of the transition temperature is a hallmark of soft, two-dimensional ferromagnetic van der Waals crystals. $Cr_2Ge_2Te_6$ is a nearly ideal two-dimensional Heisenberg ferromagnet and so will be useful for studying fundamental spin behaviours, opening the door to exploring new applications such as ultra-compact spintronics.

Atomically thin, layered van der Waals (vdW) crystals are ideal two-dimensional (2D) material systems with exceptional physical properties[11–13]. Emerging functional devices[13] (for example, ultrafast photodetectors, broadband optical modulators and excitonic semiconductor lasers) have been derived primarily from the electron-charge degree of freedom, whereas 2D spintronics[1–3,14] based on vdW crystals is still in its infancy, hindered by the lack of long-range ferromagnetic order that is crucial for macroscopic magnetic effects[4,7]. The emergence of ferromagnetism in 2D vdW crystals, if possible, combined with their rich electronics and optics, could open up numerous opportunities for 2D magnetic, magnetoelectric and magneto-optic applications[2,3].

The absence of ferromagnetic order in many 2D vdW crystals (for example, graphene or MoS_2) has motivated efforts to extrinsically induce magnetism using several methods: (i) through defect engineering, via vacancies, adatoms, grain boundaries or edges[6–10,15,16]; (ii) by introducing magnetic species via intercalation or substitution[17]; and (iii) via the magnetic proximity effect, whereby 2D materials are placed in contact with other magnetic substrates. In these schemes, it is difficult to create long-range correlation between extrinsically introduced local magnetic moments via robust exchange interaction[7], and the substrate-induced magnetic responses of 2D materials are limited. Theoretical proposals for inducing ferromagnetism by engineering the band structure[16,18,19] have yet to be realized experimentally. In contrast, if realizable, intrinsic ferromagnetism originating from the parent 2D lattice will be fundamental for understanding the underlying physics of electronic and spin processes, and for device applications.

Whether the long-range ferromagnetic order that exists in the bulk persists in the 2D regime is a fundamental question, because the strong thermal fluctuations may easily destroy the 2D ferromagnetism, according to the Mermin–Wagner theorem[5]. Fig. 1 provides an illustration of the fundamental physics of 2D ferromagnetism: the presence of a spin-wave excitation gap—a direct result of magnetic anisotropy—is essential for long-range ferromagnetic order at finite (non-zero) temperatures. Most of the ferromagnetic vdW bulk crystals reported so far are magnetically soft with small easy-axis (in the direction normal to the 2D plane) anisotropy. Harnessing long-range ferromagnetic order in 2D vdW crystals relies on the strength of the magnetic anisotropy that is retained in the 2D regime. Here we report long-range ferromagnetic order in pristine $Cr_2Ge_2Te_6$ atomic layers based on the temperature- and magnetic-field-dependent Kerr effect study via scanning magneto-optic Kerr microscopy. In our soft, 2D ferromagnetic vdW crystal, we achieve unprecedented magnetic field control of the ferromagnetic transition temperature using surprisingly small fields ($\leq$0.3 T).

Mechanical exfoliation via adhesive tape was applied to prepare $Cr_2Ge_2Te_6$ atomic layers on 260-nm-thick SiO_2/Si chips. Bulk $Cr_2Ge_2Te_6$ has been reported[20,21] to be ferromagnetic below 61 K, with an out-of-plane magnetic easy axis and negligible coercivity (Extended Data Fig. 1b, c and Methods). The monolayer was found to degrade rapidly and become invisible under an optical microscope (Extended Data Fig. 2), whereas the peeling off of bilayer flakes was repeatable and the bilayer was shown to be robust without traceable degradation in 90 min in ambient atmosphere (Extended Data Fig. 3). Therefore, the thinnest structure we studied was a bilayer. The thickness of the atomic layers is determined by the combination of optical contrast and atomic force microscopy (Extended Data Fig. 4).

The scanning Kerr microscope used was constructed with a fibre-optic Sagnac interferometer[22] with 10^{-8} rad DC Kerr sensitivity and micrometre spatial resolution, which is an ideal non-destructive optical method for imaging and measuring the magnetism of nanometre-thick and micrometre-sized flakes. The geometry of the fibre-based zero-area loop Sagnac interferometer guarantees the rejection of reciprocal effects and senses only non-reciprocal effects with high precision, thus affording a static measurement of the absolute Kerr rotation angle without sample modulations. These merits make it ideal for detecting small signals from as-exfoliated 2D flakes without involving any device fabrication process, which might perturb the intrinsic ferromagnetism. See Extended

[1]Nano-scale Science and Engineering Center (NSEC), 3112 Etcheverry Hall, University of California, Berkeley, California 94720, USA. [2]Department of Physics and Astronomy, University of California, Irvine, California 92697, USA. [3]Department of Physics, University of California, Berkeley, California 94720, USA. [4]Material Sciences Division, Lawrence Berkeley National Laboratory, 1 Cyclotron Road, Berkeley, California 94720, USA. [5]Department of Chemistry, Princeton University, Princeton, New Jersey 08540, USA.
*These authors contributed equally to this work.

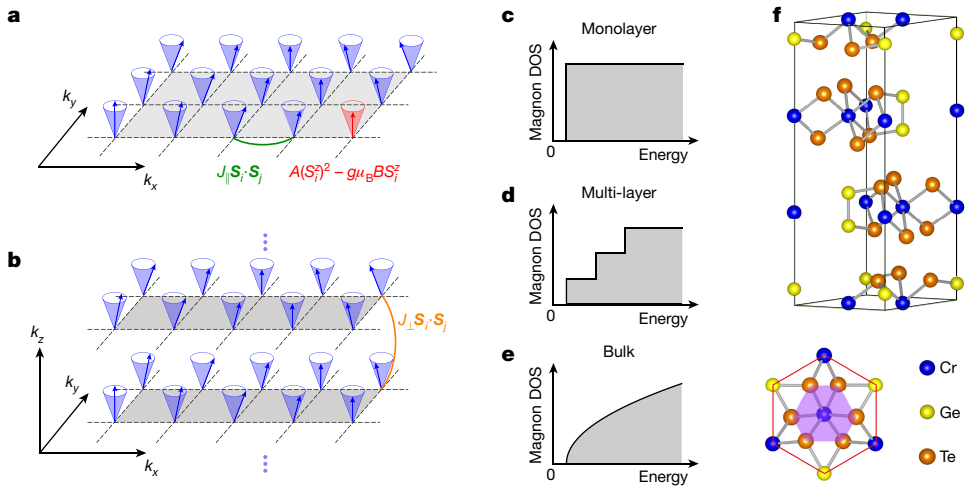

Figure 1 | Schematics of spin-wave excitations in two and three dimensions. a, **b**, Ferromagnetic spin-wave excitations in 2D (**a**) and 3D (**b**), with intralayer and interlayer exchange interactions $J_{\parallel}$ (in green) and $J_{\perp}$ (in orange), respectively, single-ion anisotropy A and magnetic field B (in red), as seen in equation (1). The cones are classical precession trajectories of thermally excited spins (arrows). **c**–**e**, Schematics of magnon density of states (DOS) per spin around the low-energy band edge of monolayer (**c**), multi-layer (**d**) and bulk (**e**) ferromagnetic materials. The low-energy excitations from the ferromagnetic ground state follow parabolic dispersions; accordingly, the DOS is a step function in 2D and proportional to $\sqrt{E}$ in 3D, where E is the excitation energy. Consequently, more magnons are excited by a given thermal energy in 2D than in 3D. In 2D, the ferromagnetic transition temperature T_C is determined primarily by the excitation gap that results from the magnetic anisotropy, whereas in 3D it is determined primarily by exchange interactions. **f**, Crystal structure (side and top views) of $Cr_2Ge_2Te_6$. Bulk $Cr_2Ge_2Te_6$ has a layered structure with interlayer vdW spacing of 3.4 Å.

Data Fig. 5 for a detailed description of the experimental set-up. In such a sensitive experiment, in which an approximately 3.5-μm light spot is focused on nanometre-thick and micrometre-sized flakes, any horizontal drifting and vertical defocusing could induce large signal fluctuations. To avoid drifting-induced variation, every Kerr-rotation data point presented here is a summary based on a scanned image that includes the target flake and the surrounding substrate, except for the bulk measurement in Fig. 2j. We also examined the magnetic properties of the bulk crystal using a superconducting quantum interference device (SQUID); see discussions later.

To observe ferromagnetism in few-layer crystals, we monitored the temperature-dependent Kerr image of the bilayer sample in Fig. 2a with the help of a small perpendicular field of 0.075 T to stabilize the magnetic moments. Strictly speaking, upon applying an external magnetic field, we might no longer have a well-defined ferromagnetic phase transition (at temperature T_C with zero field); therefore, we refer to it as a transition between a ferromagnetic-like state and a paramagnetic-like state, separated by a transition temperature T_C^*. Figure 2b–e shows the emergence of ferromagnetic order in bilayer $Cr_2Ge_2Te_6$ as temperature decreases: at 40 K, the Kerr intensity of the scanning area is hardly discernible, except in the region corresponding to thicker flakes ($\geq$3 layers); as the temperature decreases, the long strip becomes more easily recognizable; and, as the temperature approaches that of liquid helium, the long bilayer strip becomes clearly distinguishable from the surrounding bare substrate, in terms of the intensity of the Kerr rotation angle. The visibility of thicker ($\geq$3 layers) flakes at 40 K implies a higher T_C^* for thicker crystals, as we discuss further below.

The non-zero transition temperature T_C^* in the bilayer sample reflects true 2D ferromagnetic order in our system. First, the observed ferromagnetism is not due to substrate polarization because SiO_2 is non-magnetic and does not bond strongly to $Cr_2Ge_2Te_6$ layers. Second, the exposure-to-air time, from the flake exfoliation to the specimen loading in a vacuum chamber (10^{-6} torr), is strictly controlled to be less than 15 min. Even if there were ambient effects, these would generally reduce T_C^*. Therefore, the observation of finite T_C^* is unambiguous evidence of 2D ferromagnetism originating from $Cr_2Ge_2Te_6$ atomic layers.

A strong dimensionality effect is revealed by a thickness-dependent study under a 0.075-T field. Figure 2f–k displays a monotonic increase in T_C^* with increasing thickness, from a bilayer value of about 30 K to a bulk limit of about 68 K. The behaviour of T_C^* from 2D to 3D regimes is similar to the universal trend of many magnetic transition-metal thin films[23,24], although the interlayer bonding strength in vdW crystals is 2–3 orders of magnitude weaker than that of traditional metals. The strong thickness dependence of T_C^* indicates an essential role of interlayer magnetic coupling in establishing the ferromagnetic order in $Cr_2Ge_2Te_6$ crystals. In other words, ferromagnetic order in bulk vdW crystals does not guarantee ferromagnetic order in 2D sheets, highlighting the necessity of a measurement directly on atomic layers.

To gain a deeper level of understanding of the observed 2D ferromagnetic behaviour in $Cr_2Ge_2Te_6$, we study a Heisenberg Hamiltonian with magnetic anisotropies:

$$H = \frac{1}{2}\sum_{i,j} J_{ij}\boldsymbol{S}_i \cdot \boldsymbol{S}_j + \sum_i A(S_i^z)^2 - g\mu_B \sum_i BS_i^z \qquad (1)$$

in which $\boldsymbol{S}_i$ is the spin operator on site i, J_{ij} is the exchange interaction between sites i and j, A is the single-ion anisotropy, g is the Landé g-factor, μ_B is the Bohr magneton and B is the external magnetic field. To solve this spin Hamiltonian, we apply the renormalized spin-wave theory (RSWT)[25], which includes magnon–magnon scatterings at the Hartree–Fock level self-consistently (Methods). The input interaction parameters (three intralayer $J_{\parallel}$ values, three interlayer $J_{\perp}$ values and A) are calculated on the basis of an *ab initio* density functional method[26] at the local spin density approximation plus U level (Methods). We find that small onsite Hubbard U values ($U = 0.5$ eV) reproduce the magnetic ground-state properties of bulk $Cr_2Ge_2Te_6$ (Methods). The J values that are directly mapped out from first-principles density functional calculations appear to be overestimated within RSWT, and are rescaled by a fixed and uniform factor of 0.72 that reproduces the experimental bulk T_C (Methods). We perform layer-dependent calculations, including the Zeeman effect from the 0.075-T external field (Fig. 2k), assuming $A = 0$ in few-layer crystals and $A = -0.05$ meV in the bulk (Methods); we observe a strong dimensionality effect, in line with experimental observations. At finite temperatures, spontaneous symmetry breaking (ferromagnetic order) takes place in 3D for the rotationally invariant isotropic Heisenberg system ($A = 0$ and $B = 0$), but is completely suppressed by the thermal fluctuations of the long-wavelength gapless Nambu–Goldstone modes in 2D.

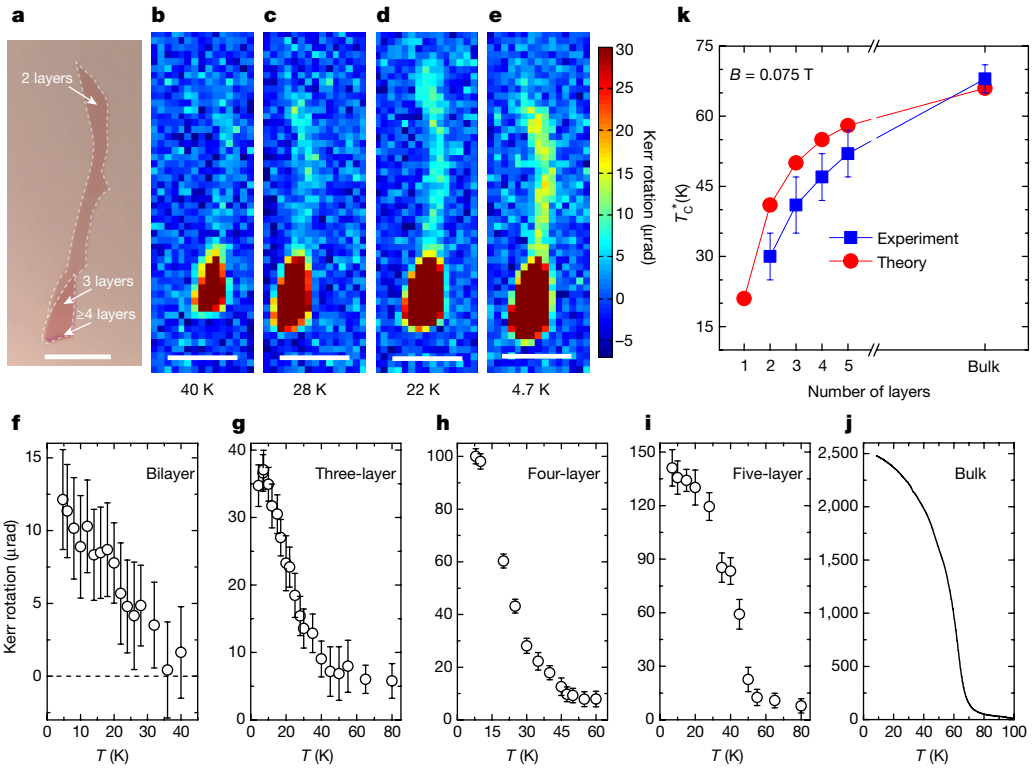

Figure 2 | Observation of ferromagnetism in bilayer $Cr_2Ge_2Te_6$ and temperature-dependent Kerr rotation of few-layer and bulk $Cr_2Ge_2Te_6$ crystals. a, Optical image of exfoliated $Cr_2Ge_2Te_6$ atomic layers on 260-nm-thick SiO_2/Si, consisting of a 31-μm-long bilayer strip attached to a thicker end (≥3 layers). **b**–**e**, The emergence of a Kerr rotation signal for the bilayer flake under 0.075 T, as the temperature decreases from 40 K to 4.7 K. The average background signal has been subtracted and the signals are truncated at 30 μrad. Scale bars in **a**–**e**, 10 μm. **f**–**j**, Temperature-dependent Kerr rotation intensities of 2–5-layer and bulk samples under a 0.075-T field. Error bars represent the standard deviation of sample signals. **k**, Transition temperatures T_C^* (defined in text) of samples of different thickness, obtained from Kerr measurements (blue squares) and theoretical calculations (red circles). A strong dimensionality effect is evident. T_C^* is determined experimentally to be the range (error bars) approximating the paramagnetic tail of the effective Kerr signal, and theoretically by the vanishing net magnetization.

Nevertheless, magnetic anisotropy ($A \neq 0$ or $B \neq 0$) could establish ferromagnetic order in 2D at finite temperatures by breaking the continuous rotational symmetry of the Hamiltonian, thereby giving rise to a non-zero excitation gap in the lowest-energy mode of the acoustic magnon branch. Thermal energy at finite T_C^* excites a large number of low-energy but finite-frequency magnon modes, flattening the expectation value of the collective spins. As the number of layers increases (from 2D to 3D), the density of states per spin for the magnon modes near the excitation gap is rapidly reduced (Fig. 1c–e), meaning that a higher T_C^* is required to ensure a sufficient population of excitations to destroy the long-range magnetic order, thus leading to a strong dimensionality effect. This picture clearly distinguishes our observed 2D ferromagnetism in a real 2D material from the quasi-2D ferromagnetism embedded in bulk materials[27], in which there is still weak out-of-plane ferromagnetic coupling and the magnon density of states is different (see Fig. 1).

The agreement between experiments and theoretical calculations that include the Zeeman effect in the Hamiltonian reveals that the external field has an important role in the observed transition temperature. To determine the effects of the external field and intrinsic anisotropy, we conducted an experimental study of the hysteresis loop on the six-layer sample at 4.7 K. The almost saturated Kerr signal at 0.6 T shows approximately 75 μrad per layer, consistent with the order of 100 μrad per layer for Cr compounds[28]. Extreme softness (about 2% zero-field remanence of the maximum Kerr signal at 0.6 T) is observed, suggesting a very small intrinsic anisotropy (<1 μeV; Methods). Two zero-field Kerr images (Fig. 3b, c) obtained after withdrawing the magnetic field from 0.6 T and from −0.6 T show small yet definitive remanence with opposite sign (Fig. 3d, e). Kerr images under decreasing-to-zero fields (Fig. 3b, f–k) show that the flake is a single ferromagnetic domain throughout. In ultrathin flakes, dipolar interaction is expected to be very small and the equilibrium domain size would probably be very large[29]. The observation of about 2% single-domain remanence is unambiguous evidence of the strong thermal fluctuations in the 2D regime, in contrast to 3D ferromagnets in which fractional remanence (if any) is usually caused by multi-domains. In another six-layer sample, we repeated a similar hysteresis loop, and found that the remanent magnetization disappears rapidly with increasing temperatures, showing an intrinsic T_C close to 10 K (Extended Data Fig. 6). We also scanned the magnetic field on bilayer and three-layer flakes at 4.7 K and did not see remanence within the detection limit.

The vanishing remanence in three-layer flakes at 4.7 K, together with the observation of $T_C^* = 41$ K under a 0.075-T field, suggests an intrinsic T_C of bilayer and three-layer $Cr_2Ge_2Te_6$ crystals below 4.7 K and strong magnetic field control of transition temperatures in our 2D magnetic systems. A field that is usually deemed to be too small to affect transition temperatures of 3D systems (for example, <0.5 T) can markedly affect the behaviour of soft, 2D ferromagnetism by opening the spin-wave excitation gap, as sketched in Fig. 1c–e. To further examine this scenario, we conducted a temperature-dependent Kerr rotation study on bilayer, three-layer and six-layer samples under two contrasting fields: 0.065 T and 0.3 T. As the field increases from 0.065 T to 0.3 T, the T_C^* value of bilayer flakes increases from 28 K to 44 K, that of three-layer flakes increases from 35 K to 49 K, and that of six-layer flakes increases from 48 K to 65 K, which is close to the bulk limit. In stark contrast, the T_C^* value in the bulk determined from SQUID measurements under fields of 0.025–0.3 T does not show clear change. Under the two fields (0.065 T and 0.3 T), the overall shift in magnetization–temperature curves in 2D layers (Fig. 4a–c) is clearly distinguished from the tail effect of a magnetic field on the critical region above T_C^*

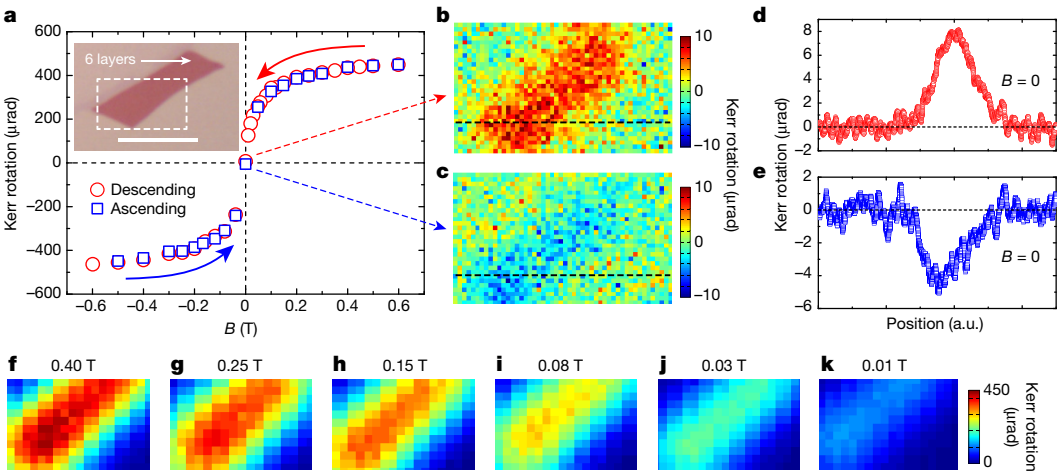

Figure 3 | Ferromagnetic hysteresis loop with single-domain remanence in a six-layer $Cr_2Ge_2Te_6$ crystal. a, Hysteresis loop of a six-layer flake at 4.7 K showing a saturating trend at 0.6 T and small non-vanishing remanence. The solid red (blue) arrow represents the descending (ascending) field. The loop starts from 0.6 T. Inset, optical image of the flake; scale bar, 10 μm. **b**, **c**, Scanned Kerr rotation images of the flake at zero field after withdrawing the field from 0.6 T (**b**) and −0.6 T (**c**). **d**, **e**, Line scanning across the flake with long acquisition time (10 times longer than for the area scanning in **b** and **c**, with each data point consequently corresponding to an average of 100 data acquisitions). The approximate line positions for **d** and **e** are indicated by black dashed lines in **b** and **c**, respectively, but extend further out of the windows (a.u., arbitrary units). The data in **b**–**e** show a clear signature of small but definitive remanent Kerr rotation angles (about 2% of the 'saturated' Kerr rotation at 0.6 T), with opposite signs on ascending and descending branches. **f**–**k**, Kerr images of the highlighted (by a dashed rectangle) area in **a**, at different descending fields, showing the persistence of a magnetic single-domain remanence. The small single-domain remanence is strong evidence that thermal fluctuations rather than the formation of multi-domains (usually in the bulk) are the reason for the reduced magnetization in our few-layer samples.

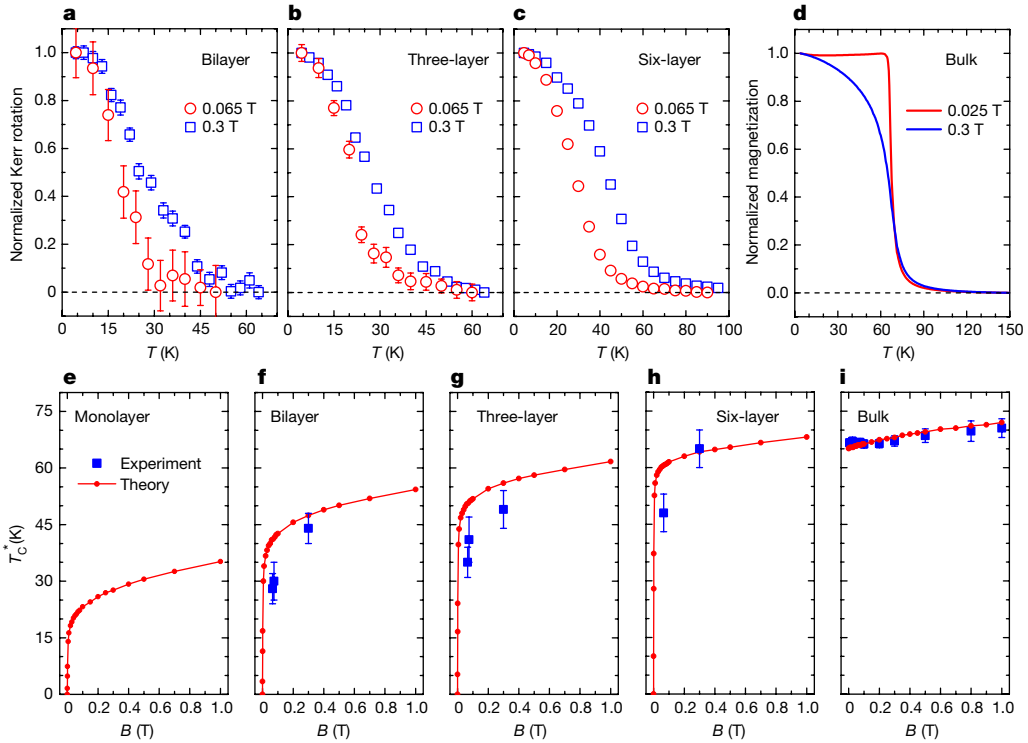

Figure 4 | Magnetic field control of the transition temperature of few-layer $Cr_2Ge_2Te_6$ crystals. a–**c**, Normalized Kerr rotation angle as a function of temperature, under two different magnetic fields: 0.065 T (red circles) and 0.3 T (blue squares), for bilayer (**a**), three-layer (**b**) and six-layer (**c**) flakes. The 0.3-T field shifts the curve markedly with respect to the curve for the 0.065-T field, indicating strong renormalization of T_C^* in few-layer $Cr_2Ge_2Te_6$. Error bars represent the standard deviation of sample signals and are smaller than the plotted point if not shown. **d**, Temperature-dependent magnetization of the bulk crystal measured by SQUID under fields of 0.025 T (red) and 0.3 T (blue). Compared with the 0.025-T field, the 0.3-T field introduces only a slightly distorted tail above T_C^*. The different behaviours below T_C^* possibly result from domains: under a 0.025-T field, multi-domains are probably formed; under a 0.3-T field, a single-domain was approached. **e**–**i**, Experimental (blue squares) and theoretical (red circles) field dependence of T_C^* in samples of various thickness. T_C^* values for the bulk crystal measured by SQUID are determined at the steepest slop of the magnetization–temperature characteristic curve. Experimental T_C^* error bars arise from the uncertainty due to the tail effect. In **f** and **g**, experimental results under a 0.075-T field (Fig. 2) are also plotted. In the 2D limit, if the single-ion anisotropy is negligibly small, the transition temperature will be very low, and can easily be tuned with a small magnetic field (for example, $B < 0.5$ T). In the bulk limit, owing to the 3D nature, such tuning is not possible.

in bulk (Fig. 4d). The possibility of superparamagnetism can be ruled out because of the integrity of the crystalline flakes, which were produced from high-quality single-phase crystals, as evidenced by X-ray diffraction[21] and transmission electron microscopy measurements[30].

The observed field effect on transition temperature can be explained well within the picture of spin-wave excitations illustrated in Fig. 1. In 2D, the ferromagnetic transition temperature depends critically on the size of the spin-wave excitation gap. In a 2D ferromagnet with negligible single-ion anisotropy, a magnetic field helps to increase the magnetic stiffness logarithmically, leading to a rapid increase in T_C^*, particularly in the range of small fields. However, in 3D, T_C^* is predominantly determined by exchange interactions, and is insensitive to small single-ion anisotropies and small fields, which are usually orders of magnitude smaller than the exchange interactions.

By means of the RSWT method, we calculated the magnetic field dependence of T_C^* in few-layer crystals and bulk. The results from the calculations are quantitatively consistent with experimental values, as shown in Fig. 4. In all of the bilayer, three-layer and six-layer samples, a remarkable change in T_C^* can be obtained over the magnetic-field range used in experiments (Fig. 4f–h); such change is not observed in the bulk (Fig. 4i). Considering the experimental challenge of determining an accurate value of the near-zero intrinsic anisotropy, we further investigated the effects of reasonably small, but finite, intrinsic anisotropies theoretically (see Methods and Extended Data Fig. 10). We find that the effect of field control on transition temperatures remains robust in this regime. For six-layer flakes under a 0.3-T field, the calculated T_C^* value approaches the bulk T_C, in agreement with experiments, thus providing an intriguing platform in which magnetic properties can easily be modulated between 2D and 3D regimes (at least with respect to the transition temperature).

We report intrinsic ferromagnetism in the 2D vdW crystal $Cr_2Ge_2Te_6$, in which a strong dimensionality effect arises from the low-energy excitations of magnons. Through the effective engineering of the magnetic anisotropy using small magnetic fields, we achieve unprecedented magnetic field control of transition temperatures in soft, 2D ferromagnetic vdW crystals. Our experimental observations are confirmed by the RSWT analysis and calculations, which may provide a generic understanding of the ferromagnetic behaviour of many soft, 2D vdW ferromagnets, such as $Cr_2Si_2Te_6$ and CrI_3. Our discovery of the soft, 2D ferromagnetic vdW crystal $Cr_2Ge_2Te_6$ provides a nearly ideal 2D Heisenberg ferromagnet for exploring fundamental physics, and opens up new possibilities for applications such as ultra-compact spintronics.

Online Content Methods, along with any additional Extended Data display items and Source Data, are available in the online version of the paper; references unique to these sections appear only in the online paper.

Received 9 June 2016; accepted 6 March 2017.
Published online 26 April 2017.

1. Han, W., Kawakami, R. K., Gmitra, M. & Fabian, J. Graphene spintronics. *Nat. Nanotechnol.* **9,** 794–807 (2014).
2. Ohno, H. *et al.* Electric-field control of ferromagnetism. *Nature* **408,** 944–946 (2000).
3. Chang, C.-Z. *et al.* Experimental observation of the quantum anomalous Hall effect in a magnetic topological insulator. *Science* **340,** 167–170 (2013).
4. Wang, Z., Tang, C., Sachs, R., Barlas, Y. & Shi, J. Proximity-induced ferromagnetism in graphene revealed by the anomalous Hall effect. *Phys. Rev. Lett.* **114,** 016603 (2015).
5. Mermin, N. D. & Wagner, H. Absence of ferromagnetism or antiferromagnetism in one- or two-dimensional isotropic Heisenberg models. *Phys. Rev. Lett.* **17,** 1133–1136 (1966).
6. Gonzalez-Herrero, H. *et al.* Atomic-scale control of graphene magnetism by using hydrogen atoms. *Science* **352,** 437–441 (2016).
7. Nair, R. R. *et al.* Spin-half paramagnetism in graphene induced by point defects. *Nat. Phys.* **8,** 199–202 (2012).
8. McCreary, K. M., Swartz, A. G., Han, W., Fabian, J. & Kawakami, R. K. Magnetic moment formation in graphene detected by scattering of pure spin currents. *Phys. Rev. Lett.* **109,** 186604 (2012).
9. Červenka, J., Katsnelson, M. I. & Flipse, C. F. J. Room-temperature ferromagnetism in graphite driven by two-dimensional networks of point defects. *Nat. Phys.* **5,** 840–844 (2009).
10. Uchoa, B., Kotov, V. N., Peres, N. M. R. & Neto, A. H. C. Localized magnetic states in graphene. *Phys. Rev. Lett.* **101,** 026805 (2008).
11. Geim, A. K. & Novoselov, K. S. The rise of graphene. *Nat. Mater.* **6,** 183–191 (2007).
12. Mak, K. F., McGill, K. L., Park, J. & McEuen, P. L. The valley Hall effect in MoS_2 transistors. *Science* **344,** 1489–1492 (2014).
13. Xia, F., Mueller, T., Lin, Y.-M., Valdes-Garcia, A. & Avouris, P. Ultrafast graphene photodetector. *Nat. Nanotechnol.* **4,** 839–843 (2009).
14. Kou, X. *et al.* Scale-invariant quantum anomalous Hall effect in magnetic topological insulators beyond the two-dimensional limit. *Phys. Rev. Lett.* **113,** 137201 (2014).
15. Jung, J., Pereg-Barnea, T. & MacDonald, A. H. Theory of interedge superexchange in zigzag edge magnetism. *Phys. Rev. Lett.* **102,** 227205 (2009).
16. Son, Y. W., Cohen, M. L. & Louie, S. G. Half-metallic graphene nanoribbons. *Nature* **444,** 347–349 (2006).
17. Dresselhaus, M. S. *Intercalation in Layered Materials* (Plenum Press, 1986).
18. Castro, E. V., Peres, N. M. R., Stauber, T. & Silva, N. A. P. Low-density ferromagnetism in biased bilayer graphene. *Phys. Rev. Lett.* **100,** 186803 (2008).
19. Cao, T., Li, Z. & Louie, S. G. Tunable magnetism and half-metallicity in hole-doped monolayer GaSe. *Phys. Rev. Lett.* **114,** 236602 (2015).
20. Carteaux, V., Brunet, D., Ouvrard, G. & Andre, G. Crystallographic, magnetic and electronic structures of a new layered ferromagnetic compound $Cr_2Ge_2Te_6$. *J. Phys. Condens. Matter* **7,** 69–87 (1995).
21. Ji, H. *et al.* A ferromagnetic insulating substrate for the epitaxial growth of topological insulators. *J. Appl. Phys.* **114,** 114907 (2013).
22. Xia, J., Beyersdorf, P. T., Fejer, M. M. & Kapitulnik, A. Modified Sagnac interferometer for high-sensitivity magneto-optic measurements at cryogenic temperatures. *Appl. Phys. Lett.* **89,** 062508 (2006).
23. Li, Y. & Baberschke, K. Dimensional crossover in ultrathin Ni(111) films on W(110). *Phys. Rev. Lett.* **68,** 1208–1211 (1992).
24. Zhang, R. & Willis, R. F. Thickness-dependent Curie temperatures of ultrathin magnetic films: effect of the range of spin-spin interactions. *Phys. Rev. Lett.* **86,** 2665–2668 (2001).
25. Bloch, M. Magnon renormalization in ferromagnets near the Curie point. *Phys. Rev. Lett.* **9,** 286–287 (1962).
26. Giannozzi, P. *et al.* QUANTUM ESPRESSO: a modular and open-source software project for quantum simulations of materials. *J. Phys. Condens. Matter* **21,** 395502 (2009).
27. Hirakawa, K. Kosterlitz-Thouless transition in two-dimensional planar ferromagnet K_2CuF_4. *J. Appl. Phys.* **53,** 1893–1898 (1982).
28. Weber, M. J. *Handbook of Optical Materials* section 1.6.3 (CRC Press, 2003).
29. Kaplan, B. & Gehring, G. A. The domain structure in ultrathin magnetic films. *J. Magn. Magn. Mater.* **128,** 111–116 (1993).
30. Alegria, L. D. *et al.* Large anomalous Hall effect in ferromagnetic insulator-topological insulator heterostructures. *Appl. Phys. Lett.* **105,** 053512 (2014).

Acknowledgements We thank J.-G. Zheng for help with AFM measurement at UC Irvine, and R. Birgeneau for providing SQUID Magnetometry at UC Berkeley. This work was primarily supported by the US Department of Energy, Office of Science, Office of Basic Energy Sciences, Materials Sciences and Engineering Division under Contract No. DE-AC02-05-CH11231 (van der Waals heterostructures program, KCWF16). The computational resource was provided by the National Energy Research Scientific Computing Center, which is supported by the US DOE. The bulk crystal growth at Princeton University was supported by the NSF MRSEC programme, grant NSF DMR-1420541, and the measurements at UC Irvine were partially supported by NSF DMR-1350122.

Author Contributions C.G. and X.Z. conceived and initiated the research and designed the experiments; C.G. performed the Sagnac MOKE measurements with assistance from L.L., A.S. and Y.X., under the guidance of J.X.; Z.L. and T.C. performed theoretical calculations under the guidance of S.G.L.; H.J. synthesized $Cr_2Ge_2Te_6$ bulk crystals under the guidance of R.J.C.; C.G. prepared and characterized few-layer samples with assistance from Y.X., W.B. and C.W.; and C.G., Z.L., T.C., Y.W., Z.Q.Q., S.G.L., J.X. and X.Z. analysed the data and wrote the paper.

Author Information Reprints and permissions information is available at www.nature.com/reprints. The authors declare no competing financial interests. Readers are welcome to comment on the online version of the paper. Publisher's note: Springer Nature remains neutral with regard to jurisdictional claims in published maps and institutional affiliations. Correspondence and requests for materials should be addressed to X.Z. (xiang@berkeley.edu), J.X. (xia.jing@uci.edu) or S.G.L. (sglouie@berkeley.edu).

METHODS

Characterizations of bulk $Cr_2Ge_2Te_6$ crystal. High-quality crystals are synthesized using the method reported in ref. 21. The soft texture and shining appearance (Extended Data Fig. 1a) indicate that the $Cr_2Ge_2Te_6$ crystal might be able to be exfoliated down to atomic layers. Magnetization characterization confirms its out-of-plane easy axis (Extended Data Fig. 1b), with a Curie temperature $T_C \approx 66$ K (Extended Data Fig. 1c). Previous work[20,21] has reported $T_C \approx 61 \pm 1$ K; the divergent values are due to the different definitions of T_C. Strictly speaking, upon applying an external magnetic field, we might no longer have a well-defined ferromagnetic phase transition; therefore, here we refer to it as a transition between a ferromagnetic-like state and a paramagnetic-like state, separated by a transition temperature T_C^*. For all of the bulk crystals characterized by SQUID, owing to the large signals and continuous sweeping of temperatures, we define T_C^* at the steepest slope; for all of the samples characterized by magneto-optic Kerr microscopy (MOKE), owing to the signal noise and the limited number of sampled temperatures, we define T_C^* as the turning points near the paramagnetic tail, with Kerr signals slightly larger than the paramagnetic tail. From a mean-field perspective, the easy-axis single-ion anisotropy A can be estimated from the saturation field $B_s \approx 0.5$ T of $B_{\parallel}$, $-AS^2 = g\mu_B B_s S/2$, where $S = 3/2$, giving an estimated $A = -0.02$ meV for bulk $Cr_2Ge_2Te_6$.

Evidence of invisible-monolayer $Cr_2Ge_2Te_6$. $Cr_2Ge_2Te_6$ thin flakes were exfoliated by adhesive tape on SiO_2/Si wafer, after which they were examined under an optical microscope. Flakes with similar optical contrasts to those indicated by white arrows in Extended Data Fig. 2a are always the thinnest achievable samples, estimated using an optical microscope. No thinner flakes are clearly found by either optical imaging or ambient atomic force microscopy (AFM). Owing to the environmental AFM applied on freshly exfoliated samples (the exposure-to-air time is shorter than 15 min), monolayer $Cr_2Ge_2Te_6$ is found near to a bilayer flake, as shown in Extended Data Fig. 2c. In Extended Data Fig. 2c, the holey monolayer film degraded, leading to invisibility under optical microscope, as shown in Extended Data Fig. 2b. Similar degradation of ultrathin flakes has been observed in several other types of vdW materials, such as TaS_2 and $NiPS_3$[31,32]. Scanning electron microscopy (SEM) also reveals the apparent presence of a degraded monolayer $Cr_2Ge_2Te_6$ flake, as indicated in Extended Data Fig. 2e.

Identification of sample thickness. The identification of $Cr_2Ge_2Te_6$ flakes is conducted on the basis of optical contrast and AFM. More than 3,000 exfoliations routinely gave the thinnest (that is, the most transparent flake in an optical image) flake, for which AFM measurement gives the thickness about 2 nm (Extended Data Fig. 2). AFM can easily overestimate the thickness for ultrathin vdW flakes because of the decoupling of the flake from the substrate, possibly due to the presence of moistures, airs or photoresist residues trapped at the flake–substrate interface. Besides the ease of overestimation, assigning a 2-nm step height to the monolayer is still risky unless there is additional unambiguous spectroscopic evidence, such as a Raman spectrum for monolayer graphene or a photoluminescence spectrum for monolayer MoS_2. As discussed above, with evidence from environmental AFM and SEM, an invisible monolayer is found and bilayers can be assigned with assurance. The ultrathin $Cr_2Ge_2Te_6$ flakes follow a linear thickness-dependent optical contrast, which has previously been observed in the low-absorption regime of many types of vdW flakes[33]. Across our large number exfoliations, the optical contrasts of bilayer and three-layer flakes have routinely been found to be within the ranges 0.22 ± 0.02 and -0.33 ± 0.03, respectively. Specifically, representative bilayer, three-layer and four-layer $Cr_2Ge_2Te_6$ flakes used in our MOKE experiments (Extended Data Fig. 4a, b) exhibit green-channel optical contrasts of -0.21, -0.31 and -0.41, respectively. Optical contrast is an efficient and reliable way to determine the thickness of ultrathin vdW flakes, and a recommended way for air-sensitive samples, such as few-layer black phosphorus[33]. The thicknesses of five- and six-layer samples are confirmed by AFM (Extended Data Fig. 4).

Air stability of bilayer $Cr_2Ge_2Te_6$. We analysed optical contrast and Raman spectra to monitor the air stability of the bilayer $Cr_2Ge_2Te_6$ crystals. The optical contrast of the bilayer flake is essentially constant for the first 90 min of exposure to air, after which there is only a slight change (Extended Data Fig. 3a). Raman spectra (Extended Data Fig. 3b) do not show observable degradation when the bilayer flake is exposed to air for 90 min. For elongated exposure (for example, 150 min), well-defined Raman peaks are still present, indicating that the excellent crystalline integrity is well preserved. The only observable change in the Raman spectra of the bilayer flake after 150 min of exposure, compared with the as-exfoliated sample, is the slight decrease in peak intensity.

Positioning of a target flake. As seen from the experimental set-up (Extended Data Fig. 5), positioning a randomly located micrometre-sized flake on a centimetre-sized chip is challenging. Special mark design can aid the efficient positioning of a specific sample. Here, positioning is by sequential scanning of the chip with pre-defined patterns (Extended Data Fig. 7a). Scanning with a large spatial interval (for example, 0.1 mm) enables the large pads to be positioned (Extended Data Fig. 7b), after which the zone of the blue square in Extended Data Fig. 7a, c is scanned with a smaller spatial interval. The target flake in between certain small pads can be identified by further zoom-in scanning.

Density functional theory calculations. First-principles calculations based on density functional theory (DFT) were performed using Quantum Espresso[26] at the local spin density approximation (LSDA) plus U level[34], with a plane-wave basis set. Projector-augmented-wave (PAW) pseudopotentials taken from PSlibrary (http://www.qe-forge.org/gf/project/pslibrary) were used with either scalar or full relativistic effects for different needs. The experimental crystal structure is adopted[20]. To treat the on-site correlation properly, we adjust the U value to reproduce the correct experimental magnetic ground state of bulk $Cr_2Ge_2Te_6$. Bulk $Cr_2Ge_2Te_6$ is a ferromagnetic insulator with easy-axis anisotropy pointing along the (111) direction, perpendicular to the vdW planes. We find that for $U < 0.2$ eV, the system becomes in-plane anisotropic; for $U > 1.7$ eV, the interlayer coupling becomes antiferromagnetic, which means that the bulk crystal becomes an antiferromagnet (Extended Data Fig. 8). Therefore, we identify the reasonable range of U values to be 0.2–1.7 eV. In our subsequent calculations, we fix $U = 0.5$ eV, which gives an easy-axis anisotropy with $A = -0.05$ meV (see below). Considering the anisotropy estimated from the bulk experiment ($A = -0.02$ meV; see discussions above), this choice of U should give relatively reasonable and stable results, considering the level of accuracy of DFT in treating this special case (with a very small energy scale).

To obtain the exchange interactions J_i from *ab initio* calculations, we adopt the four-states mapping analysis[35] to extract the magnetic coupling strength of a particular pair, avoiding interference from other sites. The conventional cell is defined in Fig. 1f, the multiples of which are constructed as supercells. We consider three intralayer $J_{\parallel}$ values and three interlayer $J_{\perp}$ values (see Extended Data Fig. 9 for the definition of J). In particular, J_1, J_{z1}, J_{z2} and J_{z3} are calculated using a $2 \times 2 \times 1$ supercell. For J_2 and J_3, instead of using bulk structures, we used a monolayer $2\sqrt{3} \times 2$ supercell. The values mapped out directly from DFT calculations are $J_1^{DFT} = -3.76$meV, $J_2^{DFT} = 0.08$ meV, $J_3^{DFT} = -0.16$ meV, $J_{z1}^{DFT} = 0.05$ meV, $J_{z2}^{DFT} = -0.12$ meV and $J_{z3}^{DFT} = -0.38$ meV. The single-ion anisotropy A is extracted by calculating the energy difference between all spins along the z direction and along the x or y directions in the bulk. Spin–orbit coupling is included by using fully relativistic pseudopotentials, yielding $A = -0.05$ meV for each spin in the bulk.

Renormalized spin-wave theory (RSWT). We define the magnetic structure as the ABC-stacking hexagonal lattice shown in Extended Data Fig. 9. There are two sublattices in one primitive cell (orange and blue balls in Extended Data Fig. 9). The Hamiltonian is

$$H = \frac{1}{2}\sum_{\boldsymbol{ll'}}\sum_{\nu\nu'} J_{\nu\nu'}^{\boldsymbol{l}-\boldsymbol{l'}} \boldsymbol{S}_{\boldsymbol{l}\nu} \cdot \boldsymbol{S}_{\boldsymbol{l'}\nu'} + \sum_{\boldsymbol{l}}\sum_{\nu} A(S_{\boldsymbol{l}\nu}^z)^2 - g\mu_B \sum_{\boldsymbol{l}}\sum_{\nu} BS_{\boldsymbol{l}\nu}^z$$

where there are N unit cells (indexed by $\boldsymbol{l}$) and n sublattices in one unit cell (indexed by $\nu = 1, 2$). By applying Fourier and Holstein–Primakoff transforms[36], we arrive at

$$H_0 = \frac{S}{2}\sum_{\nu\nu'}\sum_{\boldsymbol{k}} (J_{\nu\nu'}^{\boldsymbol{k}} b_{\boldsymbol{k}\nu}^{+} b_{\boldsymbol{k}\nu'} + J_{\nu\nu'}^{-\boldsymbol{k}} b_{\boldsymbol{k}\nu} b_{\boldsymbol{k}\nu'}^{+}) - \sum_{\nu}\left(S\tilde{J}_{\nu}^{\boldsymbol{k}=0} + 2AS - g\mu_B B\right)\sum_{\boldsymbol{k}} b_{\boldsymbol{k}\nu}^{+} b_{\boldsymbol{k}\nu} + E_0$$

$$\begin{aligned} H_1 = \frac{1}{2N}\sum_{\nu\nu'}\sum_{\boldsymbol{kk'}}\sum_{\boldsymbol{q}}\{ & J_{\nu\nu'}^{\boldsymbol{q}} b_{\boldsymbol{k'}+\boldsymbol{q},\nu}^{+} b_{\boldsymbol{k}-\boldsymbol{q},\nu'}^{+} b_{\boldsymbol{k'}\nu} b_{\boldsymbol{k}\nu'} \\ & - \frac{1}{4} J_{\nu\nu'}^{-\boldsymbol{k}+\boldsymbol{q}} b_{\boldsymbol{k'}+\boldsymbol{q},\nu}^{+} b_{\boldsymbol{k}-\boldsymbol{q},\nu'}^{+} b_{\boldsymbol{k'}\nu} b_{\boldsymbol{k}\nu} \\ & - \frac{1}{4} J_{\nu\nu'}^{-\boldsymbol{k'}} b_{\boldsymbol{k'}+\boldsymbol{q},\nu}^{+} b_{\boldsymbol{k}-\boldsymbol{q},\nu'}^{+} b_{\boldsymbol{k'}\nu} b_{\boldsymbol{k}\nu'} \\ & - \frac{1}{4} J_{\nu\nu'}^{\boldsymbol{k}} b_{\boldsymbol{k'}+\boldsymbol{q},\nu}^{+} b_{\boldsymbol{k}-\boldsymbol{q},\nu}^{+} b_{\boldsymbol{k'}\nu} b_{\boldsymbol{k}\nu'} \\ & - \frac{1}{4} J_{\nu\nu'}^{\boldsymbol{k'}+\boldsymbol{q}} b_{\boldsymbol{k'}+\boldsymbol{q},\nu}^{+} b_{\boldsymbol{k}-\boldsymbol{q},\nu'}^{+} b_{\boldsymbol{k'}\nu} b_{\boldsymbol{k}\nu'} \} \\ & + \frac{1}{N}\sum_{\nu}\sum_{\boldsymbol{kk'}}\sum_{\boldsymbol{q}} A b_{\boldsymbol{k'}+\boldsymbol{q},\nu}^{+} b_{\boldsymbol{k}-\boldsymbol{q},\nu}^{+} b_{\boldsymbol{k'}\nu} b_{\boldsymbol{k}\nu} + \sum_{\nu}\sum_{\boldsymbol{k}} A b_{\boldsymbol{k},\nu}^{+} b_{\boldsymbol{k}\nu} \end{aligned}$$

where

$$J_{\nu\nu'}^{\boldsymbol{k}} = \sum_{\boldsymbol{l}-\boldsymbol{l'}} \mathrm{e}^{-i\boldsymbol{k}\cdot(\boldsymbol{l}-\boldsymbol{l'})} J_{\nu\nu'}^{\boldsymbol{l}-\boldsymbol{l'}} = J_{\nu'\nu}^{-\boldsymbol{k}}$$

$$\tilde{J}_{\nu}^{\boldsymbol{k}=0} = \sum_{\boldsymbol{l}-\boldsymbol{l'}}\sum_{\nu'} J_{\nu\nu'}^{\boldsymbol{l}-\boldsymbol{l'}} = \sum_{\nu'} J_{\nu\nu'}^{\boldsymbol{k}=0}$$

and

$$E_0 = \frac{1}{2}\sum_{ll'}\sum_{\nu\nu'} J_{\nu\nu'}^{l-l'} S^2 + \sum_{l}\sum_{\nu} AS^2 - g\mu_B \sum_{l}\sum_{\nu} BS$$

is the ferromagnetic ground state energy, $S = 3/2$ for a Cr ion, $\boldsymbol{k}$, $\boldsymbol{k}'$, $\boldsymbol{q}$ are wave vectors, and $b_{\boldsymbol{k}\nu}^{+}$ and $b_{\boldsymbol{k}\nu}$ are creation and annihilation operators of a magnon with wave vector $\boldsymbol{k}$ on sublattice ν. H_0 (the non-interacting Hamiltonian) comes from the original Hamiltonian H up to second-order real-space Bosonic creation and annihilation operators (Fourier transforms of $b_{\boldsymbol{k}\nu}^{+}$ and $b_{\boldsymbol{k}\nu}$). H_1 (the interacting Hamiltonian) comes from the fourth-order terms of the real-space operators.

To obtain the spin-wave spectrum, considering the equations of motion, for a given $b_{\boldsymbol{k}_0\nu_0}$:

$$\begin{aligned}
[b_{\boldsymbol{k}_0\nu_0}, H] &= [b_{\boldsymbol{k}_0\nu_0}, H_0] + [b_{\boldsymbol{k}_0\nu_0}, H_1] \\
&= S\sum_{\nu} J_{\nu_0\nu}^{\boldsymbol{k}_0} b_{\boldsymbol{k}_0\nu} - (S\tilde{J}_{\nu_0}^{\boldsymbol{k}=0} + 2AS - g\mu_B B) b_{\boldsymbol{k}_0\nu_0} \\
&+ \frac{1}{N}\sum_{\boldsymbol{k}} (J_{\nu_0\nu_0}^{\boldsymbol{k}-\boldsymbol{k}_0} - J_{\nu_0\nu_0}^{\boldsymbol{k}}) \langle b_{\boldsymbol{k}\nu_0}^{+} b_{\boldsymbol{k}\nu_0}\rangle b_{\boldsymbol{k}_0\nu_0} \\
&+ \frac{1}{N}\sum_{\nu}\sum_{\boldsymbol{k}} J_{\nu_0\nu}^{0} \langle b_{\boldsymbol{k}\nu}^{+} b_{\boldsymbol{k}\nu}\rangle b_{\boldsymbol{k}_0\nu_0} \\
&- \frac{1}{2N}\sum_{\nu}\sum_{\boldsymbol{k}} (J_{\nu_0\nu}^{\boldsymbol{k}_0} \langle b_{\boldsymbol{k}\nu}^{+} b_{\boldsymbol{k}\nu}\rangle + J_{\nu_0\nu}^{\boldsymbol{k}_0} \langle b_{\boldsymbol{k}\nu_0}^{+} b_{\boldsymbol{k}\nu_0}\rangle) b_{\boldsymbol{k}_0\nu} \\
&+ \frac{1}{N}\sum_{\boldsymbol{k}} 4A \langle b_{\boldsymbol{k}\nu_0}^{+} b_{\boldsymbol{k}\nu_0}\rangle b_{\boldsymbol{k}_0\nu_0} + A b_{\boldsymbol{k}_0\nu_0}
\end{aligned}$$

where we have applied the Hartree–Fock approximation[25]. The spin-wave spectrum $\hbar\omega$ is the eigenvalues of this matrix.

To estimate T_C (or T_C^* under magnetic field), we consider the temperature-dependent magnetization, which follows Bose–Einstein statistics owing to the Bosonic nature of magnons. The ratio of magnetization M and the saturation magnetization M_0 is

$$\frac{M}{M_0} = 1 - \frac{1}{nNS}\sum_{\pm}\sum_{\boldsymbol{k}}\left[\exp\left(\frac{\hbar\omega_{\pm}}{k_B T}\right) - 1\right]^{-1}$$

where '$\pm$' represents the two magnon branches due to the two sublattices (Extended Data Fig. 9), and T_C is defined when $M/M_0 = 0$. The layer dependence is included by introducing discrete values of k_z due to the spatial confinement[37]. We find that the spectrum depends on the magnon population and therefore the temperature, which stems from the spin-wave interactions in H_1. Such a renormalization leads to the spin-wave softening effect in the high-temperature region close to T_C, and needs to be solved self-consistently. We find that the renormalization correction is crucial for predicting T_C values that would be overestimated by linear spin-wave theory, in which spin-wave interactions are overlooked.

Input parameters for RSWT calculations. Using the set of J^{DFT} parameters, we derive a bulk T_C of 90 K from RSWT, the same order of magnitude as the experimental value of 66 K, demonstrating the reliability of the *ab initio* RSWT method. However, considering the need for accuracy in this work, which involves logarithmically diverging behaviour, and the uncertainty in the parameters mapped out from DFT, we use an overall factor of 0.72 to rescale all of the exchange interactions so that the theoretical bulk T_C (65 K) is pinned to that of experiment (66 K from our SQUID measurements). Consequently, the exchange interactions used for all calculations are $J_1 = -2.71$ meV, $J_2 = 0.058$ meV, $J_3 = -0.115$ meV, $J_{z1} = 0.036$ meV, $J_{z2} = -0.086$ meV and $J_{z3} = -0.27$ meV.

Single-ion anisotropy in the bulk is taken as $A = -0.05$ meV, as a result of the choice of $U = 0.5$ eV, whereas $A = -0.02$ meV is estimated from experiment. For layered $Cr_2Ge_2Te_6$, the value of A cannot be determined definitively by DFT, because such a small quantity is very sensitive to possible changes in structure, layer-dependent U values, and so on; consequently, we choose the value of A according to experimental facts, while using the same set of exchange parameters (rescaled), because they are less sensitive to those factors. For the six-layer sample from experiment, about 2% single-domain remanence suggest a very small anisotropy of <1 μeV, estimated by spin-wave formalism. For simplicity, the calculations in the main text are based on $A = 0$.

To consolidate our claim that small magnetic fields largely control the transition temperature in the 2D layers, we also consider other A values (Extended Data Fig. 10). We plot the x axis (magnetic field) on a logarithmic scale. Finite single-ion anisotropies give rise to finite zero-field T_C. However, even if we consider $A = -0.01$ meV (half the estimated experimental bulk value), we still obtain a very large range of tunable T_C^* in the 2D layers. These results confirm the efficient magnetic field control of transition temperature in 2D $Cr_2Ge_2Te_6$ crystals. The results in Extended Data Fig. 10 show a crossover between the $A = 0$ and $A \neq 0$ curves; this is due to the temperature renormalization affecting the effective A, but not B.

Data availability. The data that support the findings of this study are available from the corresponding author on reasonable request.

31. Yu, Y. *et al.* Gate-tunable phase transitions in thin flakes of 1T-TaS_2. *Nat. Nanotechnol.* **10,** 270–276 (2015).
32. Kuo, C.-T. *et al.* Exfoliation and Raman spectroscopic fingerprint of few-layer $NiPS_3$ van der Waals crystals. *Sci. Rep.* **6,** 20904 (2016).
33. Li, L. *et al.* Direct observation of the layer-dependent electronic structure in phosphorene. *Nat. Nanotechnol.* **12,** 21–25 (2017).
34. Cococcioni, M. & de Gironcoli, S. Linear response approach to the calculation of the effective interaction parameters in the LDA+U method. *Phys. Rev. B* **71,** 035105 (2005).
35. Xiang, H., Lee, C., Kooc, H.-J., Gong, X. & Whangbo, M.-H. Magnetic properties and energy-mapping analysis. *Dalton Trans.* **42,** 823–853 (2013).
36. Holstein, T. & Primakoff, H. Field dependence of the intrinsic domain magnetization of a ferromagnet. *Phys. Rev.* **58,** 1098–1113 (1940).
37. Corciovei, A. Spin-wave theory of ferromagnetic thin films. *Phys. Rev.* **130,** 2223–2229 (1963).

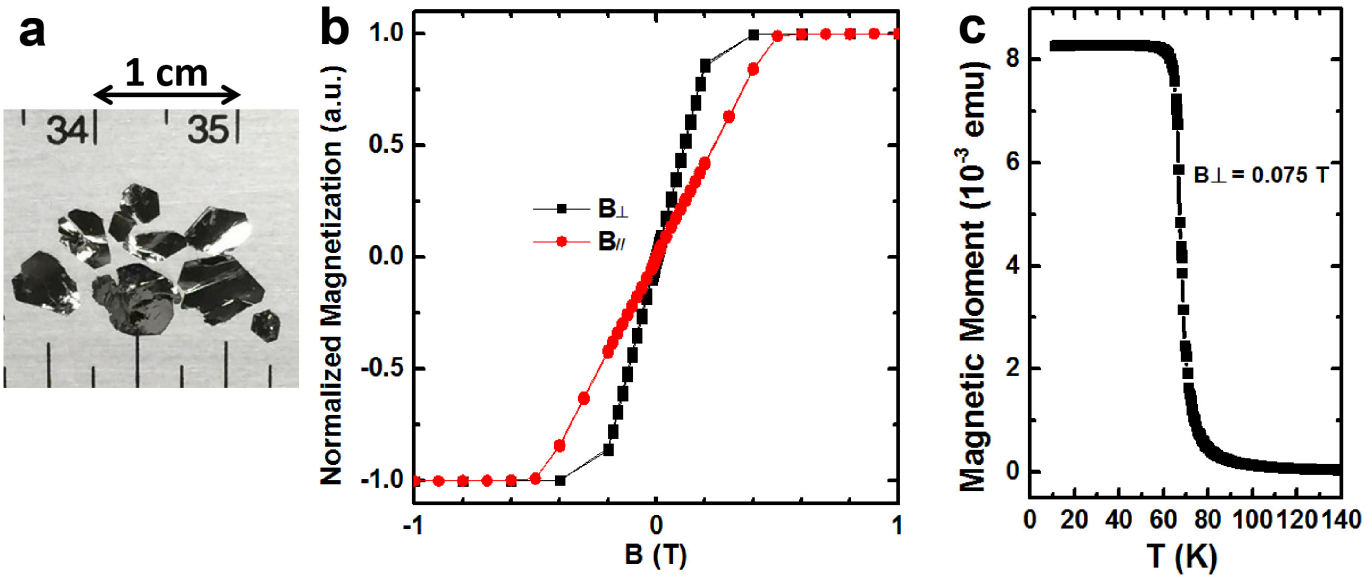

Extended Data Figure 1 | Magnetization characterizations of a bulk $Cr_2Ge_2Te_6$ crystal. a, Photo of bulk $Cr_2Ge_2Te_6$ platelets. **b**, Magnetization characterization by SQUID at 4 K, showing that $Cr_2Ge_2Te_6$ has an out-of-plane easy axis. **c**, Temperature-dependent magnetization characterization under a 0.075-T out-of-plane field, showing $T_C^* \approx 66$ K by SQUID, consistent with our Kerr rotation result ($T_C^* \approx 68$ K; in Fig. 2j).

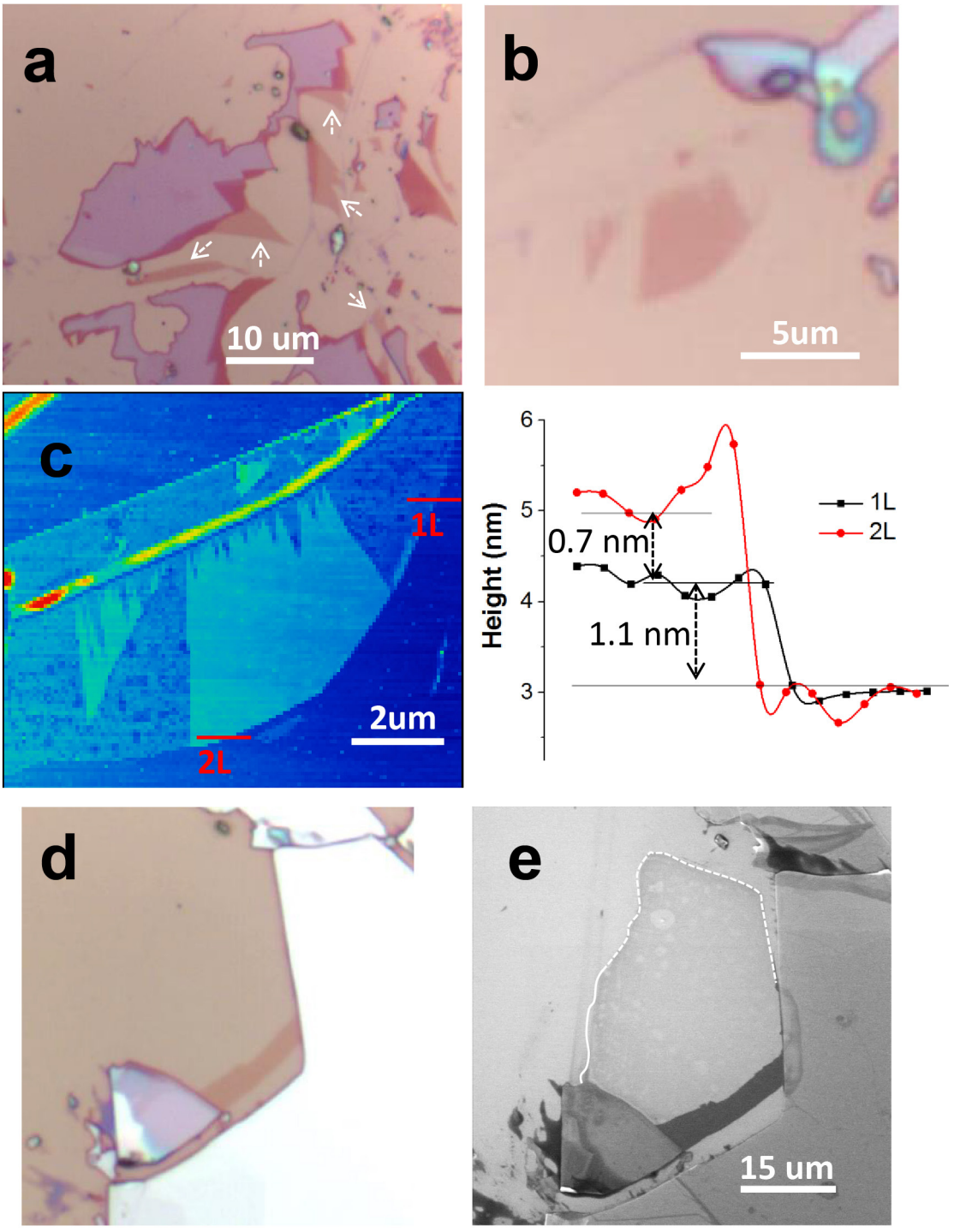

Extended Data Figure 2 | Characterizations of monolayer and bilayer $Cr_2Ge_2Te_6$ flakes. a, A representative optical image of exfoliated bilayer flakes. White arrows point to bilayer flakes. **b**, An optical image of a specific bilayer flake. **c**, The environmental AFM image of the bilayer flake in **b**, showing that a large monolayer flake attaches to the bilayer flake (left). The corresponding AFM height profiles are also shown (right). **d, e**, Optical (**d**) and SEM (**e**) images of thin $Cr_2Ge_2Te_6$ flakes. The SEM image reveals an additional flake (circled by a white dashed line in **e**, adjacent to the bilayer strip), which might be a degraded monolayer flake (degradation can be seen from the bubble-like features).

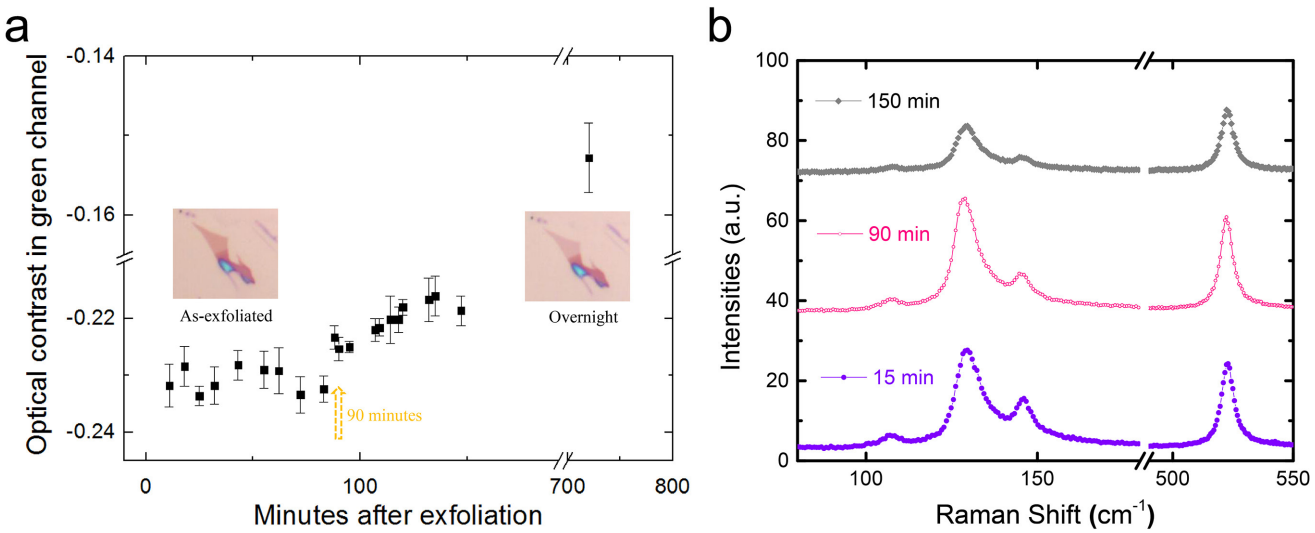

Extended Data Figure 3 | Evolution of optical contrast and Raman spectra of bilayer $Cr_2Ge_2Te_6$ flakes in air. a, Evolution of optical contrast of a bilayer $Cr_2Ge_2Te_6$ flake in air. After 90 min of exposure to air (highlighted by the yellow dashed arrow), the optical contrast of the bilayer flake begins to reduce slowly. Error bars are the standard deviation of the optical contrast of the flake of various regions. Insets show optical images of the flake as freshly exfoliated and after overnight exposure in air. **b**, The evolution of the Raman spectra of another bilayer $Cr_2Ge_2Te_6$ flake**.** To avoid laser-triggered degradation, Raman spectra were acquired when the sample was pumped back to vacuum (10^{-5}–10^{-6} torr). The peaks in the range 100–150 cm^{-1} are features of bilayer $Cr_2Ge_2Te_6$ and the peak at 520 cm^{-1} is from Si.

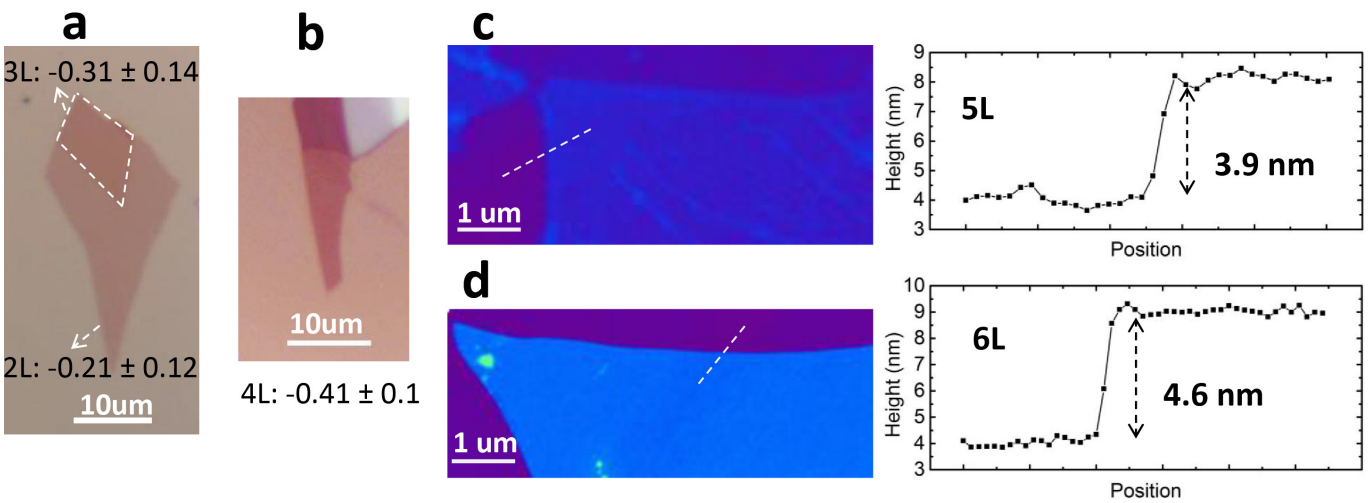

Extended Data Figure 4 | Optical and AFM images of few-layer samples. a, **b**, Optical images of bilayer (2L) and three-layer (3L) flakes (**a**) and a four-layer (4L) flake (**b**). Numbers in **a** and **b** are the optical contrasts in the green channel of the flakes; errors are standard deviations. **c**, **d**, AFM images of five-layer (5L; **c**) and six-layer (6L; **d**) samples, with the corresponding height profiles.

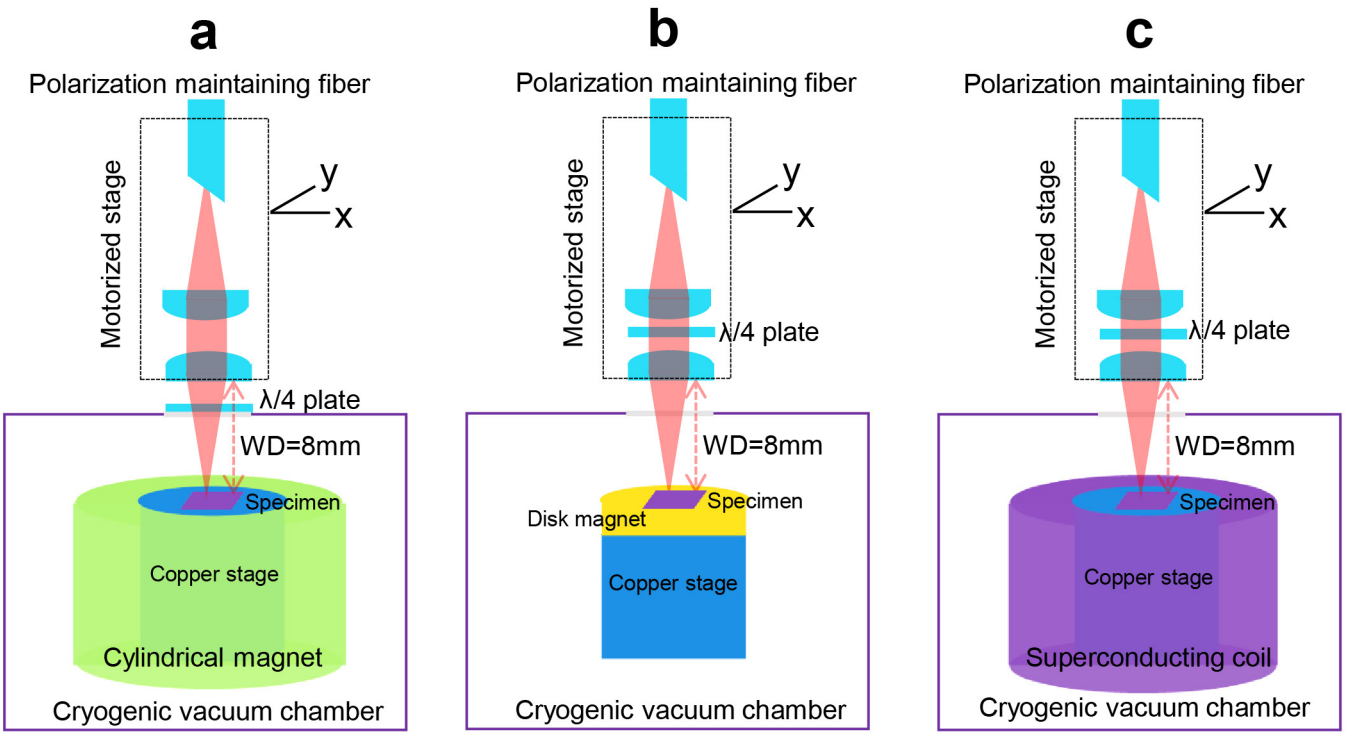

Extended Data Figure 5 | The sample-end experimental set-up of Sagnac MOKE. a, For the temperature-dependent Kerr image study of 2–5-layer samples under a 0.075-T field, the specimen is loaded on a stage surrounded by a cylindrical permanent magnet and the effective magnetic field perpendicular to the specimen surface is approximately 0.075 T, measured by a Gauss meter. A quarter wave plate is placed on the quartz window. Therefore, the raw signal includes a sample Kerr rotation signal and a background signal, primarily from the Faraday effect of the quartz window. The background signal can readily be obtained by data acquisition on the bare SiO_2 substrate. A description of the remaining part of the optical set-up connecting to the polarization maintaining fibre can be found in ref. 22. **b**, For the study of magnetic field control of transition temperatures, a slightly modified experimental set-up is used. The cylindrical magnet in **a** provides a magnetic field of only very limited strength. To compare the contrasting fields, we machined the heights of copper stages to accommodate the heights of different disk magnets with contrasting field strengths: 0.065 T and 0.3 T. **c**, For the hysteresis study, we made a superconducting coil to accommodate the chamber. Owing to the connection between the superconducting coil and the sample stage in our set-up, the superconducting coil cannot be used for temperature-dependent studies. WD, working distance.

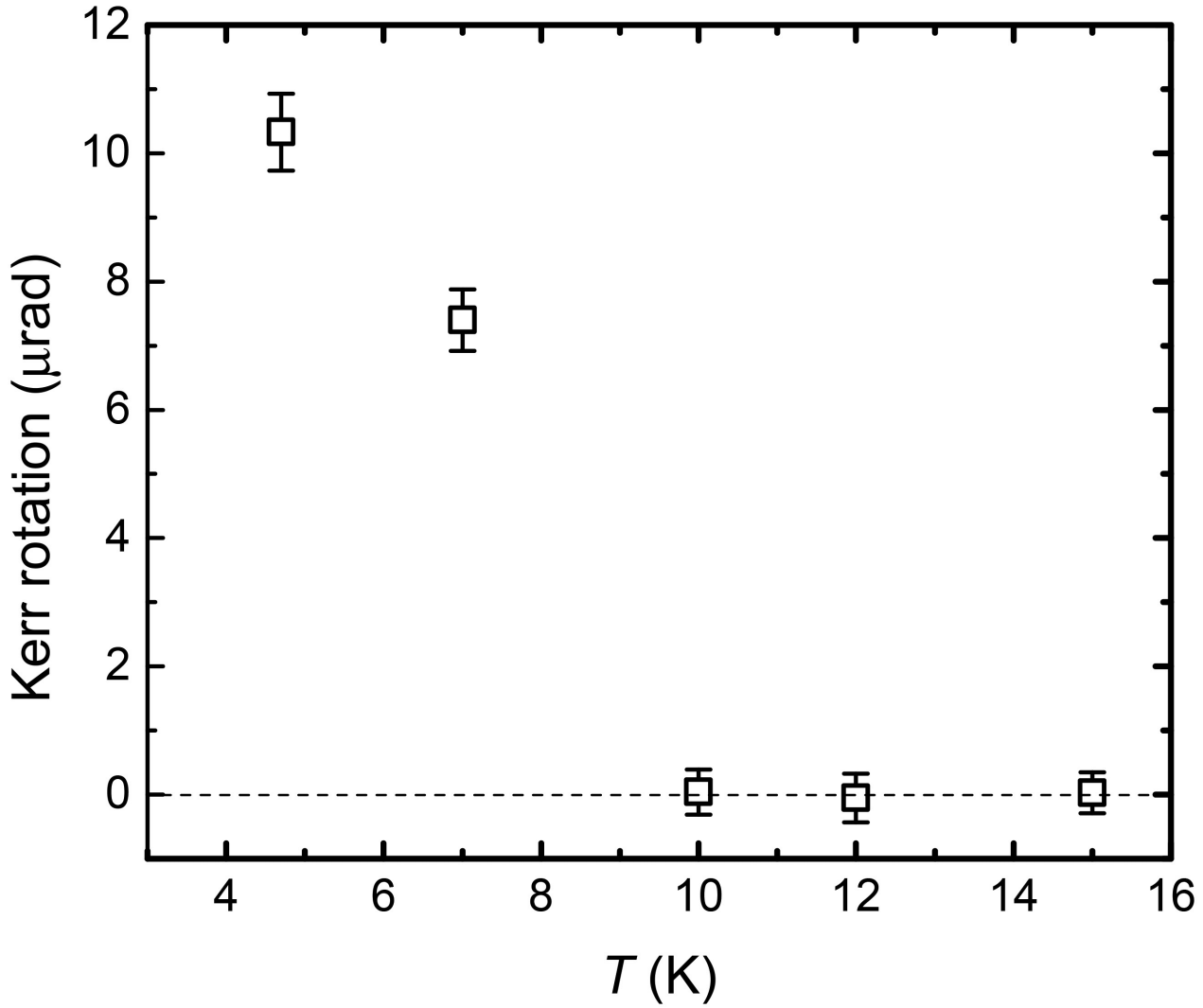

Extended Data Figure 6 | Temperature evolution of the remanent magnetization of a six-layer $Cr_2Ge_2Te_6$ flake. At 4.7 K, after 'saturating' the six-layer $Cr_2Ge_2Te_6$ flake by a 0.6-T magnetic field, the remanent magnetization is obtained by removing the field. Subsequently, under zero-field, the temperature is increased, during which process the Kerr rotation angle is tracked. This measurement shows an intrinsic ferromagnetic phase transition temperature of a six-layer $Cr_2Ge_2Te_6$ flake close to 10 K. Error bars, standard error of sample signals.

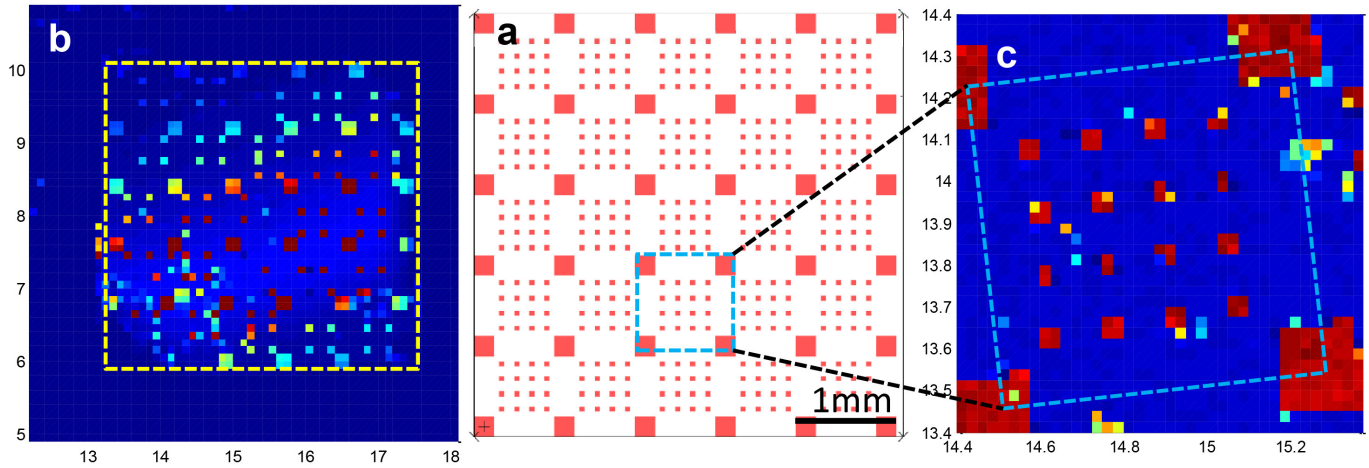

Extended Data Figure 7 | Positioning a target flake. a, The pre-defined patterns of metal pads. **b**, A scanned map of the reflectance of the specimen. The colour represents the reflected light intensity. The reflectance of metal pads can vary because some pads were peeled off during the exfoliation process. **c**, A smaller-size scanning. The units of the numbers on the axes in **b** and **c** are millimetres.

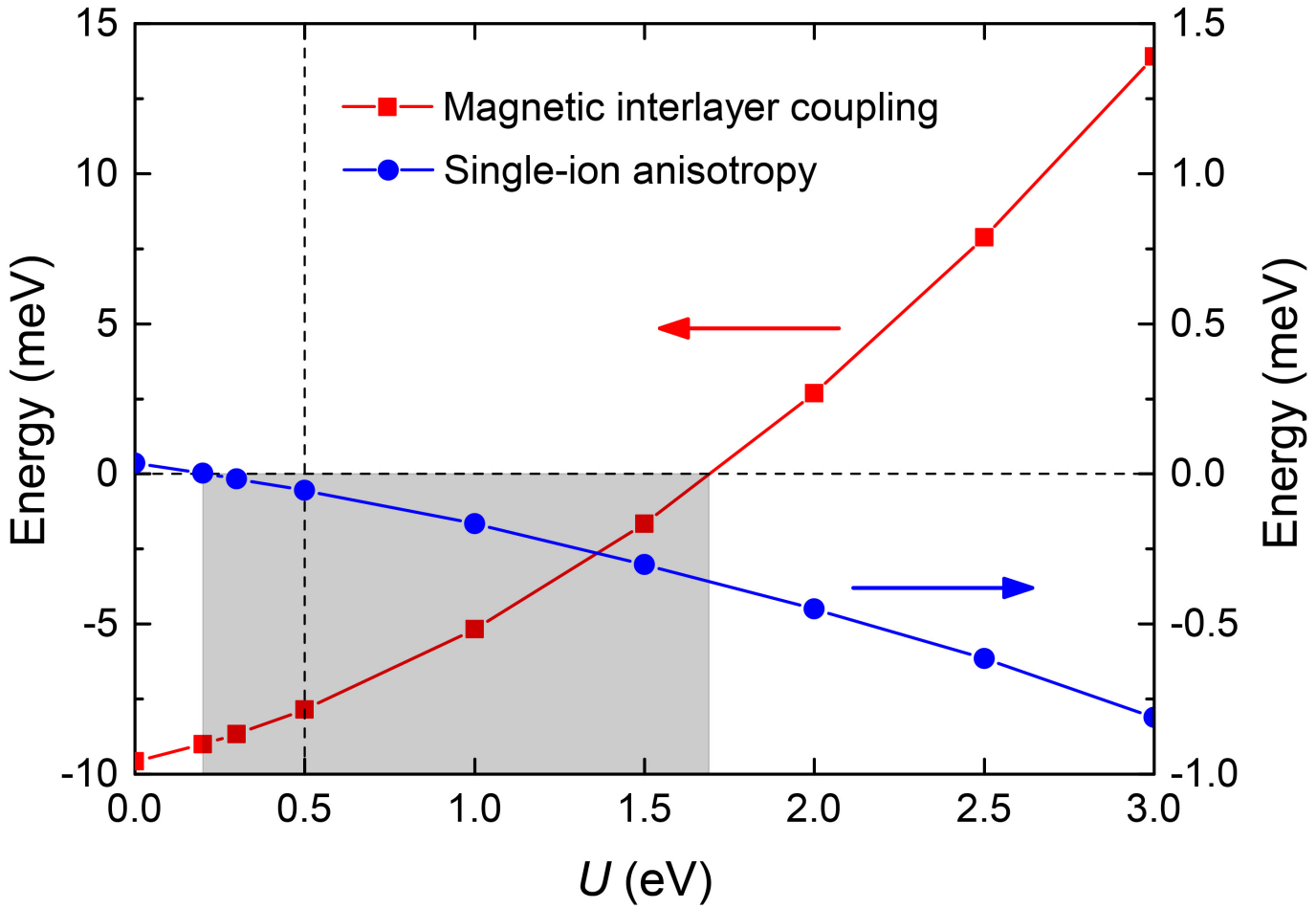

Extended Data Figure 8 | Magnetic interlayer coupling and single-ion anisotropy as a function of on-site Hubbard U in bulk $Cr_2Ge_2Te_6$. Blue circles represent single-ion anisotropy, and the magnetic anisotropy is out-of-plane (negative single-ion anisotropy) for $U > 0.2$ eV. Red squares represent interlayer magnetic coupling, which is ferromagnetic (negative) for $U < 1.7$ eV. Bulk $Cr_2Ge_2Te_6$ is a ferromagnet with an out-of-plane easy axis. Therefore, the range $0.2\,\text{eV} < U < 1.7\,\text{eV}$ (shaded area) could qualitatively reproduce the bulk magnetic property. We set $U = 0.5$ eV in the subsequent calculations, because the experimentally estimated single-ion anisotropy in the bulk is small.

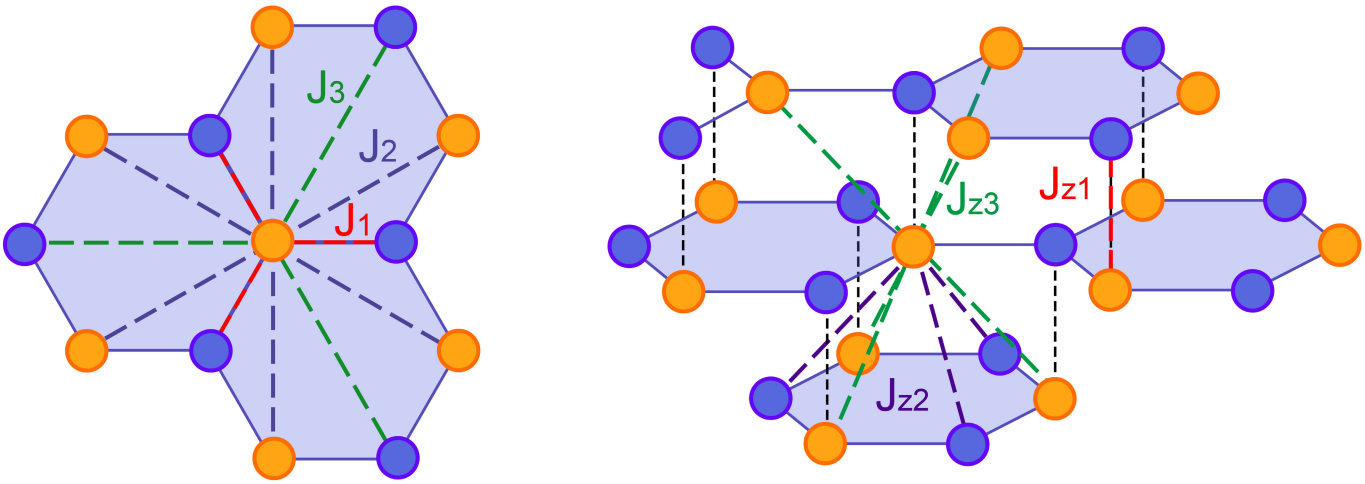

Extended Data Figure 9 | Crystal structure consisting of magnetic ion Cr only. Illustration of in-plane (left) and out-of-plane (right) nearest-neighbour exchange interactions. The ABC-type stacked hexagonal lattice is a reduced illustration of atomic arrangement of Cr in bulk $Cr_2Ge_2Te_6$ crystals. J_1, J_2 and J_3 (J_{z1}, J_{z2} and J_{z3}) represent the first, second and third in-plane (out-of-plane) nearest-neighbour spin–spin exchange interactions, respectively. Positive and negative J values represent antiferromagnetic and ferromagnetic exchange interactions. Each Cr site carries a spin $S = 3/2$ in theoretical simulations. Blue and orange circles represent the Cr ions on A and B sublattices, respectively.

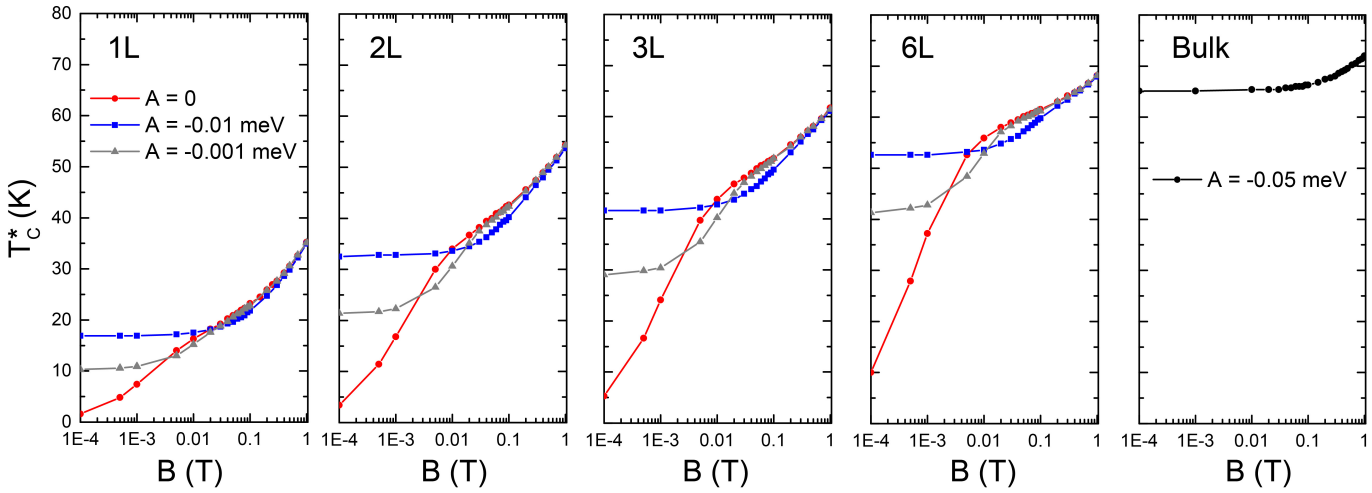

Extended Data Figure 10 | Magnetic-field-dependent T_C^* under different values of anisotropy in RSWT. Calculated magnetic-field-dependent T_C^* of monolayer (1L), bilayer (2L), three-layer (3L) and six-layer (6L) samples using $A = 0$, $A = -0.01$ meV and $A = -0.001$ meV in RSWT, as well as that of the bulk, with $A = -0.05$ meV. The x axis (B field) is plotted on a logarithmic scale. The efficient field control of transition temperature is clearly seen for small anisotropies in 2D layers.